Title
Integration of a continuum damage model for shale with the cutting plane algorithm

Journal
International Journal for Numerical and Analytical Methods in Geomechanics, 41(4)

ISSN
0363-9061

Authors
Xu, Hao
Prévost, Jean H

Publication Date
2017-03-01

DOI
10.1002/nag.2563

Peer reviewed

Integration of a continuum damage model for shale with the cutting plane algorithm

Hao Xu

Jean H. Prévost
First published: 20 August 2016
https://doi.org/10.1002/nag.2563
Cited by: 1
UC-eLinks

Summary

The stability of integration is essential to numerical simulations especially when solving nonlinear problems. In this work, a continuum damage mechanics model proposed by the first author is implemented with an integration method named cutting plane algorithm (CPA) to improve the robustness of the simulation. This integration method is one type of return mapping algorithm that bypasses the need for computing the gradients. We compare the current integration method with the previous direct method, and the result shows that the cutting plane algorithm exhibits excellent performance under large loading rate conditions. To enhance accuracy of the new method, a control procedure is utilized in the implementation of the algorithm based on error analysis. Thereafter, the theory of poromechanics is utilized with the damage model to account for the effects of fluid diffusion. Laboratory tests simulated with finite element method illustrate distinct behaviors of shale with different loading rates and indicate the development of microcrack propagation under triaxial compression.

1 Introduction

Cracks are associated with rocks and other brittle materials. Continuum damage mechanics (CDM) is utilized to capture microcrack initialization and propagation in solids 1, 2. The initial idea of damage variable was first introduced by Kachanov 3 to account for the degradation of mechanical properties of materials under creep conditions. Then CDM has been widely used in brittle materials, such as concretes 4, 5 and rocks 6-8. Damage effects are analyzed at the scale of a representative elementary volume element, which avoids to consider families of microcracks evolution simultaneously and makes it well suited for numerical implementation in finite element methods (FEMs). A phenomenological model to predict damage-induced anisotropy in rocks was proposed by the author 9. However, to implement a non-linear constitutive model for a material in FEM is always a challenge. Isotropic and anisotropic damage models proposed by different authors are many 7, 10-12, but successful implementations in FEM, especially with anisotropic damage, are rare 13, 14. The integration method used in solving nonlinear stress–strain history of materials is commonly proposed for plasticity or viscoplasticity 15, 16. Sloan has proposed a

modified Euler scheme for numerical integration 17. It has been improved with automatic error control 18 and been utilized for unsaturated soils 19. However, the essential of the explicit method relies on the determination of the yield surface. The complexity of the nonlinear constitutive model and loading conditions increases the difficulty of this process. The implicit method can avoid this issue by bypassing the point or using one type of return mapping algorithm. Normally, trial elastic stress–strain relations are first evaluated, which are subsequently mapped to a suitably updated yield surface. However, this integration method is restricted to simple plasticity models with linear hardening and constant isotropic elastic moduli 20. The damage model utilized here exhibits a nonlinear elastic response, a non-associated damage evolution, and a complex yield criterion. If a classical integration method is used, the task of evaluating gradients of the hardening of the yield surface and potential surface is overwhelming. The strategy implemented here, named cutting plane algorithm, bypasses the need for computing the gradients, and it is applicable to general materials with non-associated flow rules and arbitrary yield criteria.

Experimental and numerical studies on rocks show that effects of pore pressures play important roles on determining the strength of rocks under saturated or unsaturated conditions. The undrained response of rocks has been studied in references 21, 22 with triaxial compression experiments, while Islam and Skalle investigate shale mechanical properties through both drained and undrained tests 23. Pore pressures in their works are measured during tests and are analyzed with Skempton's coefficient 24. A more realistic representation of fluid pressures is to model the coupling between hydraulic and mechanical processes 25, in which the interaction between solid matrix and the fluid is required 26. In this work, we use the modern theory of poromechanics (e.g., Coussy 27) to study the effects of fluid diffusion in rocks as well as the damage propagation with CDM model.

The conceptual expression of CDM model is summarized in Section 2 as well as its implementation with the cutting plane algorithm. In Section 3, the comparison between the new algorithm and the previous method comes to the conclusion that the stability is improved. Errors due to large loading rates are estimated, and a strategy is provided in the implementation to increase accuracy. Section 4 simulates an axisymmetric example of a plug test with FEM and investigates the damage evolution in shales. Section 5 studies further the damage propagation with fluid diffusion effects in 3D models. Distinct loading conditions corresponding to various loading rates are taken into account in the simulations of laboratory experiments.

2 Constitutive Model and Implementation

2.1 Continuum damage model

2.1.1 Constitutive equations of the skeleton [9], [28]

The proposed anisotropic damage model named deviatoric stress-induced damage (DSID) model is hyperelastic, that is, the stress–strain relationship derives from the expression of a thermodynamic potential. The free energy utilized in this model is Gibbs free energy, whose general form was introduced into CDM with the concept of effective stress to account for the reduction of undamaged areas [29]. Hayakawa and Murakami have formulated a different expression that is linearly dependent on damage variable $\boldsymbol{\Omega}$, and a modified stress tensor is proposed to represent closure effects of microcracks [11]. DSID model is based on the energy expression Shao *et al.* proposed, which is similar as Hayakawa and Murakami's. But this equation depends on Cauchy stress tensor, so it avoids discontinuous differential in integration process [30].

$$G_s = \frac{1+\nu_0}{2E_0}\mathrm{Tr}(\boldsymbol{\sigma}^2) - \frac{\nu_0}{2E_0}(\mathrm{Tr}\boldsymbol{\sigma})^2 + a_1\,\mathrm{Tr}(\boldsymbol{\Omega})(\mathrm{Tr}\boldsymbol{\sigma})^2 + a_2\,\mathrm{Tr}(\boldsymbol{\sigma}\cdot\boldsymbol{\sigma}\cdot\boldsymbol{\Omega}) + a_3\,\mathrm{Tr}(\boldsymbol{\sigma})\mathrm{Tr}(\boldsymbol{\Omega}\cdot\boldsymbol{\sigma}) + a_4\,\mathrm{Tr}(\boldsymbol{\Omega})\mathrm{Tr}(\boldsymbol{\sigma}\cdot\boldsymbol{\sigma}) \quad (1)$$

where E_0 and ν_0 are the initial Young's modulus and Poisson's ratio, respectively; $\boldsymbol{\sigma}$ is the Cauchy stress; $\boldsymbol{\Omega}$ is the damage tensor, defined as the second-order crack density tensor [3]; and a_i are material parameters for the free energy. In this article, we use general mechanical sign convention, which means tension is positive while compression is negative. The damage driving force is obtained by deriving G_s by the damage tensor:

$$\boldsymbol{Y} = \frac{\partial G_s}{\partial \boldsymbol{\Omega}} = a_1(\mathrm{Tr}\boldsymbol{\sigma})^2\,\boldsymbol{\delta} + a_2\boldsymbol{\sigma}\cdot\boldsymbol{\sigma} + a_3\mathrm{Tr}(\boldsymbol{\sigma})\boldsymbol{\sigma} + a_4\mathrm{Tr}(\boldsymbol{\sigma}\cdot\boldsymbol{\sigma})\boldsymbol{\delta} \quad (2)$$

The total elastic strain $\boldsymbol{\varepsilon}^E$ is obtained by deriving G_s by the Cauchy stress $\boldsymbol{\sigma}$:

$$\boldsymbol{\varepsilon}^E = \frac{\partial G_s}{\partial \boldsymbol{\sigma}} = \frac{1+\nu_0}{E_0}\boldsymbol{\sigma} - \frac{\nu_0}{E_0}(\mathrm{Tr}\boldsymbol{\sigma})\boldsymbol{\delta} + 2a_1\,[\mathrm{Tr}(\boldsymbol{\Omega})(\mathrm{Tr}\boldsymbol{\sigma})]\boldsymbol{\delta} + a_2\,(\boldsymbol{\sigma}\cdot\boldsymbol{\Omega} + \boldsymbol{\Omega}\cdot\boldsymbol{\sigma}) + a_3[\mathrm{Tr}(\boldsymbol{\sigma}\cdot\boldsymbol{\Omega})\boldsymbol{\delta} + (\mathrm{Tr}\boldsymbol{\sigma})\boldsymbol{\Omega}] + 2a_4(\mathrm{Tr}\boldsymbol{\Omega})\boldsymbol{\sigma} \quad (3)$$

and it contains two parts:

$$\boldsymbol{\varepsilon}^E = \boldsymbol{\varepsilon}^{el} + \boldsymbol{\varepsilon}^{ed} \quad (4)$$

in which $\boldsymbol{\varepsilon}^{el}$ is the purely elastic strain, which would be recovered by unloading, and $\boldsymbol{\varepsilon}^{ed}$ is the additional elastic strain induced by the degradation of stiffness. Therefore, total strain $\boldsymbol{\varepsilon}$ can be decomposed as

$$\boldsymbol{\varepsilon} = \boldsymbol{\varepsilon}^E + \boldsymbol{\varepsilon}^{id} = \boldsymbol{\varepsilon}^{el} + \boldsymbol{\varepsilon}^{ed} + \boldsymbol{\varepsilon}^{id} \quad (5)$$

$\boldsymbol{\epsilon}^{id}$ is the irreversible strain, induced by residual crack openings existing in a sample after a release of loading stress (additional compression is needed to close the cracks and to get back to a state of zero deformation) 12.

2.1.2 Damage function

The expression of the damage function is written in the following form:

$$f_d = \sqrt{J^*} - \alpha I^* - k \tag{6}$$

J^* and I^* are defined as

$$J^* = \frac{1}{2}\left(\mathbb{P}_1 : \boldsymbol{Y} - \frac{1}{3} I^* \boldsymbol{\delta}\right) : \left(\mathbb{P}_1 : \boldsymbol{Y} - \frac{1}{3} I^* \boldsymbol{\delta}\right), \quad I^* = (\mathbb{P}_1 : \boldsymbol{Y}) : \boldsymbol{\delta} \tag{7}$$

where $\mathbb{P}_1$ is a fourth-order projection tensor defined as

$$\mathbb{P}_1(\boldsymbol{\sigma}) = \sum_{p=1}^{3} \left[H\left(\sigma^{(p)}\right) - H\left(-\sigma^{(p)}\right) \right] \boldsymbol{n}^{(p)} \otimes \boldsymbol{n}^{(p)} \otimes \boldsymbol{n}^{(p)} \otimes \boldsymbol{n}^{(p)} \tag{8}$$

where $H(\cdot)$ is the Heaviside distribution function, $\boldsymbol{\sigma}^{(p)}$ is the p^{th} eigenvalue of the stress tensor, $\boldsymbol{n}^{(p)}$ is the vector aligned with the p^{th} principal direction of stress, and α is a material parameter accounting for the aperture of the cone in the $\mathbb{P}_1 : \boldsymbol{Y}$ space. The threshold k in Equation 6 is defined as a linear function of damage:

$$k = C_0 + C_1 \mathrm{Tr}(\boldsymbol{\Omega}) \tag{9}$$

where C_0 is the initial threshold of damage and C_1 controls the damage hardening.

2.1.3 Damage potential

In order to enforce the constraint on the eigenvalues of damage tensor to be non-negative, it is proposed to define the damage potential as a homogeneous function of degree one in $\boldsymbol{Y}$:

$$g_d = \sqrt{\frac{1}{2}(\mathbb{P}_2 : \boldsymbol{Y}) : (\mathbb{P}_2 : \boldsymbol{Y})} - C_2 \tag{10}$$

The projection tensor, $\mathbb{P}_2$, is introduced to represent both ‘crossing’ and ‘splitting’ effects 9:

$$\mathbb{P}_2 = \sum_{p=1}^{3} H\left[\sigma^{(p)} - \min_{q=1}^{3}\left(\sigma^{(q)}\right)\right] \boldsymbol{n}^{(p)} \otimes \boldsymbol{n}^{(p)} \otimes \boldsymbol{n}^{(p)} \otimes \boldsymbol{n}^{(p)} \tag{11}$$

2.1.4 Flow rule

Damage evolution law is obtained by calculating

$$\mathrm{d}\boldsymbol{\Omega} = \lambda \frac{\partial g}{\partial \boldsymbol{Y}} \quad (12)$$

where λ is the Lagrangian multiplier accounting for the magnitude of the damage increment. Analytical solutions for elementary mechanical tests shows that the irreversible strain $\boldsymbol{\epsilon}^{id}$ is better predicted when derived from a non-associated flow rule:

$$\mathrm{d}\boldsymbol{\varepsilon}^{id} = \lambda \frac{\partial f_d}{\partial \boldsymbol{\sigma}} = \lambda \frac{\partial f_d}{\partial \boldsymbol{Y}} \frac{\partial \boldsymbol{Y}}{\partial \boldsymbol{\sigma}} \quad (13)$$

2.2 Implementation

The damage model was originally implemented with the direct method (Picard method) solving for Lagrangian multiplier. However, convergence problems often happened. In order to solve this issue, the new version changes the integration method to cutting plane algorithm for solving nonlinear equations. Through this modification, we can have a stable method to obtain results for the simulation. All these implementations are based on the strain-controlled strategy, which is typically utilized in the programming of FEM. A trial calculation is tested with a new strain increment based on elastic assumption. If the yield condition is reached, the cutting plane algorithm is utilized to drive the stress status back to the yield surface; if the yield condition is not reached, state variables are updated using the elastic solution.

2.3 Cutting plane algorithm

The cutting plane algorithm, first proposed in Reference 31, is one type of return mapping algorithm and follows in a straightforward manner from the theory of operator splitting applied to nonlinear constitutive relations. Following the procedure of the algorithm summarized in 15, we can derive all the equations for DSID model. From Equation 5, the rate of the strain can be decomposed as

$$\mathrm{d}\boldsymbol{\varepsilon} = \mathrm{d}\boldsymbol{\varepsilon}^{E} + \mathrm{d}\boldsymbol{\varepsilon}^{id} \quad (14)$$

Equation 4 can be rewritten as

$$\boldsymbol{\varepsilon}^{E} = \mathbb{S}(\boldsymbol{\Omega}) : \boldsymbol{\sigma} \quad (15)$$

where $\mathbb{S}$ is the compliance of the material. The increment of the total elastic strain can be obtained by taking the derivative of Equation 15:

$$\mathrm{d}\boldsymbol{\varepsilon}^{E} = \mathbb{S} : \mathrm{d}\boldsymbol{\sigma} + \boldsymbol{\sigma} : \partial_{\boldsymbol{\Omega}}\mathbb{S} : \mathrm{d}\boldsymbol{\Omega} \quad (16)$$

Therefore, the increment of the stress can be computed as

$$\begin{aligned} \mathrm{d}\boldsymbol{\sigma} &= \mathbb{S}^{-1} : \left[\mathrm{d}\boldsymbol{\varepsilon}^{E} - \boldsymbol{\sigma} : \partial_{\boldsymbol{\Omega}} \mathbb{S} : \mathrm{d}\boldsymbol{\Omega} \right] \\ &= \mathbb{S}^{-1} : \mathrm{d}\boldsymbol{\varepsilon} - \mathbb{S}^{-1} : \left[\mathrm{d}\boldsymbol{\varepsilon}^{id} + \boldsymbol{\sigma} : \partial_{\boldsymbol{\Omega}} \mathbb{S} : \mathrm{d}\boldsymbol{\Omega} \right] \end{aligned} \tag{17}$$

Bring the flow rule (Equations 12 and 13) into the previous equation; the increment of the stress can be expressed as

$$\mathrm{d}\boldsymbol{\sigma} = \mathbb{S}^{-1} : \mathrm{d}\boldsymbol{\varepsilon} - \lambda\, \mathbb{S}^{-1} : [\partial_{\boldsymbol{\sigma}} f + \boldsymbol{\sigma} : \partial_{\boldsymbol{\Omega}} \mathbb{S} : \partial_{\boldsymbol{Y}} g] \tag{18}$$

Linearize the yield function at the current iteration step, we obtain

$$f_{n+1}^{(i+1)} \approx f_{n+1}^{(i)} + \partial_{\boldsymbol{\sigma}} f_{n+1}^{(i)} : \left[\boldsymbol{\sigma}_{n+1}^{(i+1)} - \boldsymbol{\sigma}_{n+1}^{(i)} \right] + \partial_{\boldsymbol{\Omega}} f_{n+1}^{(i)} : \left[\boldsymbol{\Omega}_{n+1}^{(i+1)} - \boldsymbol{\Omega}_{n+1}^{(i+1)} \right] = 0 \tag{19}$$

By discretizing Equation 18, we obtain

$$\boldsymbol{\sigma}_{n+1}^{(i+1)} - \boldsymbol{\sigma}_{n+1}^{(i)} = -\lambda_{n+1}^{(i)} \mathbb{S}_{n+1}^{-1} : \left[\partial_{\boldsymbol{\sigma}} f_{n+1}^{(i)} + \boldsymbol{\sigma}_{n+1}^{(i)} : \partial_{\boldsymbol{\Omega}} \mathbb{S}_{n+1}^{(i)} : \partial_{\boldsymbol{Y}} g_{n+1}^{(i)} \right] \tag{20}$$

The flow rule (Equation 12) indicates that the damage increment can be discretized as

$$\boldsymbol{\Omega}_{n+1}^{(i+1)} - \boldsymbol{\Omega}_{n+1}^{(i)} = \lambda_{n+1}^{(i)} \partial_{\boldsymbol{Y}} g_{n+1}^{(i)} \tag{21}$$

Taking Equations 18 and 21 into Equation 19, we obtain

$$\lambda_{n+1}^{(i)} = \frac{f_{n+1}^{(i)}}{\partial_{\boldsymbol{\sigma}} f_{n+1}^{(i)} : \mathbb{S}^{-1} : \left[\partial_{\boldsymbol{\sigma}} f_{n+1}^{(i)} + \boldsymbol{\sigma}_{n+1}^{(i)} : \partial_{\boldsymbol{\Omega}} \mathbb{S}_{n+1}^{(i)} : \partial_{\boldsymbol{Y}} g_{n+1}^{(i)} \right] - \partial_{\boldsymbol{\Omega}} f_{n+1}^{(i)} : \partial_{\boldsymbol{Y}} g_{n+1}^{(i)}} \tag{22}$$

The main algorithm for this continuum damage mechanical model is summarized in Table 1.

Table 1. Cutting plane algorithm.

1. Initialize

$$\boldsymbol{\sigma}_{n+1}^{tr} = \boldsymbol{\sigma}_n + \mathbb{S}^{-1} \cdot \mathrm{d}\boldsymbol{\varepsilon}_{n+1}$$

$$\boldsymbol{\sigma}_{n+1}^{(0)} = \boldsymbol{\sigma}_{n+1}^{tr}, \quad \boldsymbol{\varepsilon}_{n+1}^{id(0)} = \boldsymbol{\varepsilon}_n^{id}, \quad \boldsymbol{\Omega}_{n+1}^{(0)} = \boldsymbol{\Omega}_n, \quad \lambda_{n+1}^{(0)} = 0$$

2. Compute yield function

$$f_{n+1}^{(i)} = f\left[\boldsymbol{\sigma}_{n+1}^{(i)}, \boldsymbol{\Omega}_{n+1}^{(i)}\right]$$

IF $f_{n+1}^{(i)} \leq$ TOL THEN: *EXIT*

ELSE:

3. Compute increment to Lagrangian Multiplier

$$\lambda_{n+1}^{(i)} = \frac{f_{n+1}^{(i)}}{\partial_{\boldsymbol{\sigma}} f_{n+1}^{(i)} : \mathbb{S}^{-1} : \left[\partial_{\boldsymbol{\sigma}} f_{n+1}^{(i)} + \boldsymbol{\sigma}_{n+1}^{(i)} : \partial_{\boldsymbol{\Omega}} \mathbb{S}_{n+1}^{(i)} : \partial_{\boldsymbol{\Omega}} g_{n+1}^{(i)}\right] - \partial_{\boldsymbol{\Omega}} f_{n+1}^{(i)} : \partial_{\boldsymbol{Y}} g_{n+1}^{(i)}}$$

4. Update state variables

$$\boldsymbol{\varepsilon}_{n+1}^{p(i+1)} = \boldsymbol{\varepsilon}_{n+1}^{p(i)} + \lambda_{n+1}^{(i)} \partial_{\boldsymbol{\sigma}} f_{n+1}^{(i)}$$

$$\boldsymbol{\Omega}_{n+1}^{(i+1)} = \boldsymbol{\Omega}_{n+1}^{(i)} + \lambda_{n+1}^{(i)} \partial_{\boldsymbol{Y}} g_{n+1}^{(i)}$$

$$\boldsymbol{\sigma}_{n+1}^{(i+1)} = \boldsymbol{\sigma}_{n+1}^{(i)} - \lambda_{n+1}^{(i)} \mathbb{S}^{-1} : \left[\partial_{\boldsymbol{\sigma}} f_{n+1}^{(i)} + \boldsymbol{\sigma} : \frac{\partial \mathbb{S}}{\partial \boldsymbol{\Omega}} : \partial_{\boldsymbol{Y}} g_{n+1}^{(i)}\right]$$

Set $i \leftarrow i + 1$ and GO TO 2

ENDIF

Note that this algorithm is based on a forward integration of the rate equations, which is not unconditionally stable in general. However, according to our implementation experience, it works well in all cases. The cutting plane algorithm replaces the previous direct method [14], [32]and solves the nonlinear equations for the stress–strain relationship. Comparing the results between the two methods, we obtain that the same answer that proves the cutting plane algorithm is implemented correctly. The disadvantage of the direct method in our previous version [14], [32] is that when the number of loading steps is decreased (i.e., the size of the loading rate is increased), the computation is not convergent, or infinite loop may happen during iterations. These unstable issues have been resolved by the cutting plane algorithm. The accuracy and stability of the method will be discussed in the next sections.

3 Material Model Tests

3.1 Comparison between two methods

Deviatoric stress-induced damage model can be used for different types of tests, such as shear, uniaxial compression, or uniaxial tension tests. All tests results exhibit linear elasticity and non-linear damaged behavior. Because different tests display similar behaviors, for simplicity, here we only present simulation results of uniaxial compressions. We use a deviatoric strain loading as the boundary loading condition in all tests, in which the total strain is −2%. The loading rate $\Delta\epsilon_{33}$ can be different when we investigate the stability or accuracy of the computations. The parameters used in the simulations are listed in Table 2 from References 7, 30.

Table 2. Parameters in deviatoric stress-induced damage model for material tests.

Elastic parameters			**Free energy**					**Damage function**		
E_0	ν_0		a_1	a_2	a_3	a_4		C_0	C_1	α (-)
MPa	**-**		**MPa^{-1}**	**MPa^{-1}**	**MPa^{-1}**	**MPa^{-1}**		**MPa**	**MPa**	**-**
6.8E4	0.21		1.26E-7	3.94E-5	−1.26 E-6	2.51E-6		0.11	2.2	0.231

3.1.1 Convergent results

The uniaxial compression test is simulated with a small loading rate ($\Delta\epsilon_{33}$=−0.002%) for previous direct method and current cutting plane method, and the stress–strain curve obtained by each method is plotted in Figure 1. If the magnitude of the strain rate is smaller than 0.002%, the difference of all results are negligible. Therefore, the results obtained with $\Delta\epsilon_{33}$=−0.002% by both methods are convergent. We can also confirm that we implement the cutting plane algorithm correctly, and it provides the same accuracy when loading rate is quite small. As Figure 1 displays, when the strain accumulates to −0.135%, the damage threshold is reached, and cracks start to open. Before the material reaches the yield point, the material is elastic, and the stress–strain curve is linear. After damage occurs, the material stiffness is reduced because of the crack opening, and the stress–strain response becomes nonlinear.

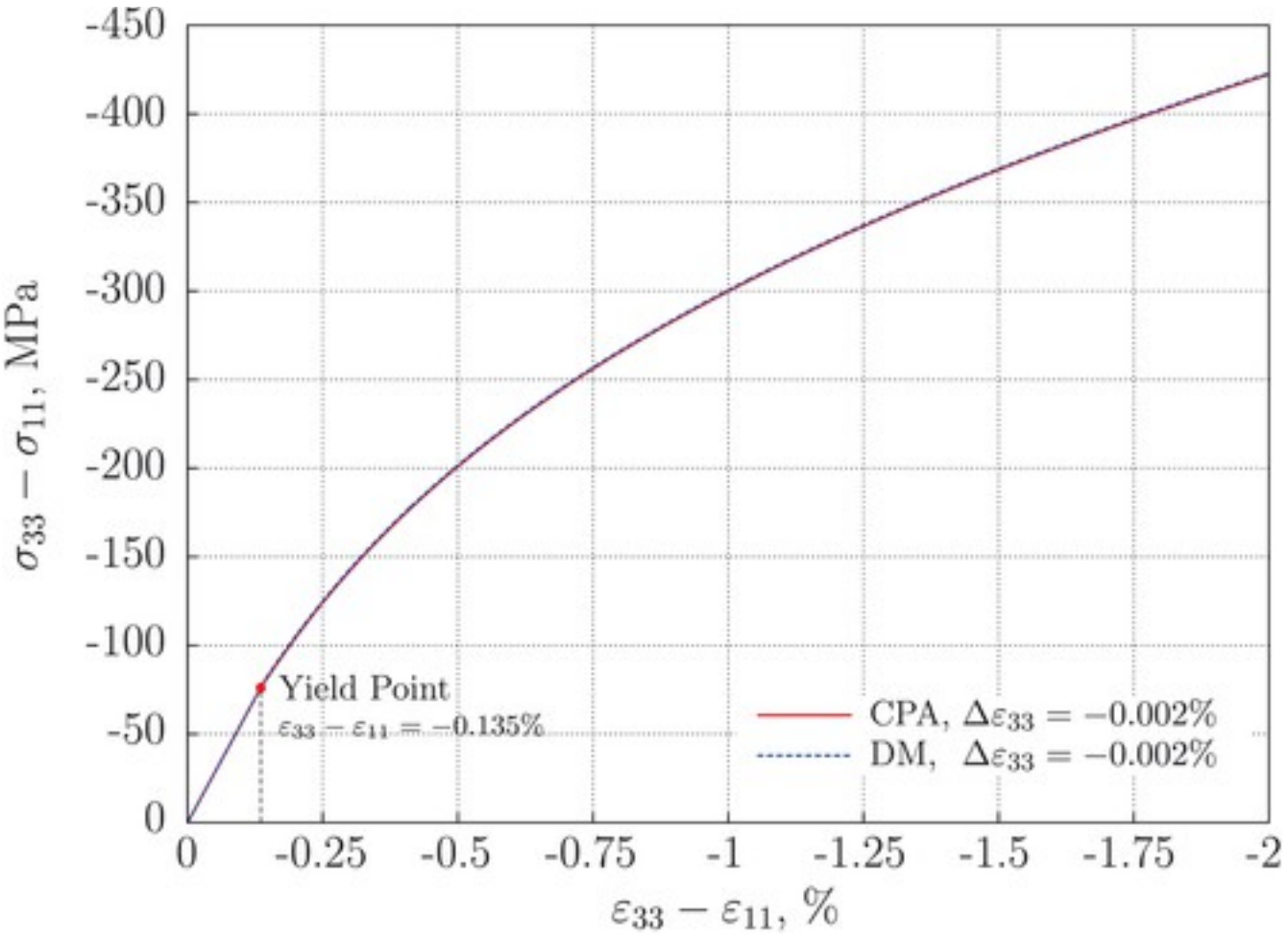

Figure 1

Open in figure viewerPowerPoint

Uniaxial compression test results with $\Delta\epsilon_{33}$=−0.002% loading rate by two methods. [Colour figure can be viewed at wileyonlinelibrary.com]

Caption

3.1.2 Accuracy and stability

It is well known that, for nonlinear problems when the magnitude of the loading rate (or time step) is larger, the computation becomes less accurate and less stable. The number of iterations may increase as well because of the complexity of the nonlinear computation. Here, we apply two additional loading rates ($\Delta\epsilon_{33}$=−0.2% and $\Delta\epsilon_{33}$=−0.04%) for the uniaxial compression tests. The convergent line is calculated with a very small loading rate by cutting plane method. Compared with the results of two methods, we can conclude the following:

- Stability. As Figure 2 shows, the computation with −0.2% loading rate by the direct method is not stable any more. It suffers from infinite iterations, and no results are obtained under this loading condition. However, the cutting plane method does not have this issue,

although the accuracy is not accurate. The direct method overestimates the stress, so the status of the material may locate above the damage yield surface, which can be the reason of the unstable issue. Different from the direct method, cutting plane method underestimates the stress and overestimates the softness of the material, which helps the model lies below the yield surface. Therefore, the cutting plane algorithm is more stable than the direct method when loading rate is large.

- Accuracy. For the case with −0.04% loading rate, we calculated the final stress difference between two methods and the convergent result. The error of the direct method is 1.1%while the error of the cutting plane method is 2.2%. The direct method is more precise than cutting plane method. Actually, with other loading rates, the accuracy of the direct method is always better than the new algorithm. Therefore, we analyze the error of the cutting plane method in the next section and propose a control procedure to improve the accuracy.

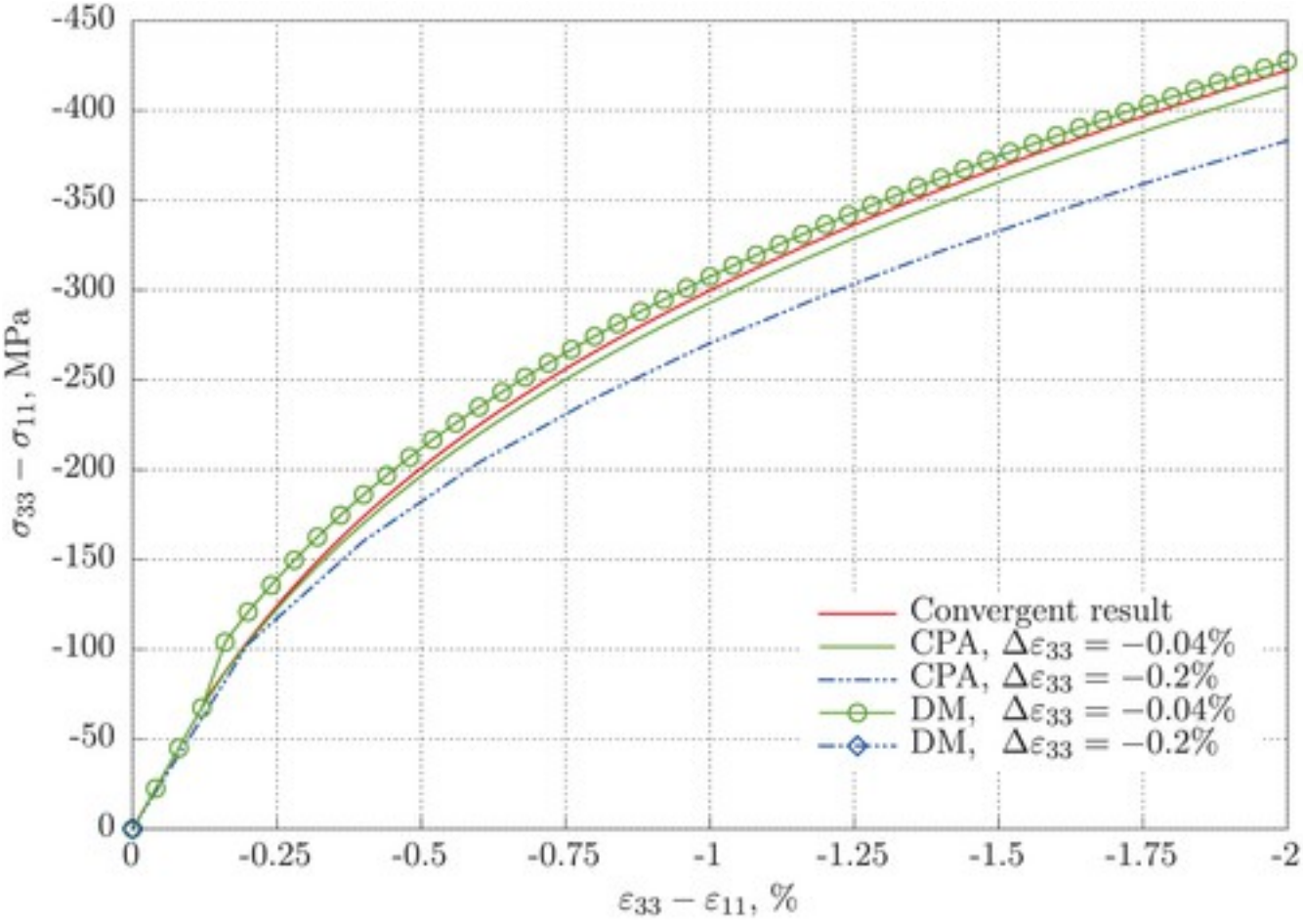

Figure 2
Open in figure viewerPowerPoint
Uniaxial compression test results with different loading rates by two methods. [Colour figure can be viewed at wileyonlinelibrary.com]
Caption

3.2 Accuracy of CPA

In order to illustrate how the strain rate affects the accuracy of simulation results with the cutting plane algorithm, we launch four cases with different loading rates ($\Delta\epsilon_{33}$=−1%, −0.2%, −0.02%, and −0.002%). All tests are simulated to a cumulative −2% deviatoric strain. Figure 3displays the stress–strain curves obtained from these four tests and exhibits the influence of loading rates on the results of these tests. The main conclusions are summarized as follows:

- Smaller loading rates result in higher accuracy. The simulation result with $\Delta\epsilon_{33}$=−0.02% is close to the one with $\Delta\epsilon$ =− 0.002%. The deviation between these two is acceptable. The loading rate $\Delta\epsilon_{33}$=−0.002% can be considered as the convergent result. Compared with that case, the difference of other cases are 1.0%, 9.4%, and 29.2%, respectively.
- With larger loading rates, the accuracy of the simulation is lower, but the trend of the curve still keeps the same.

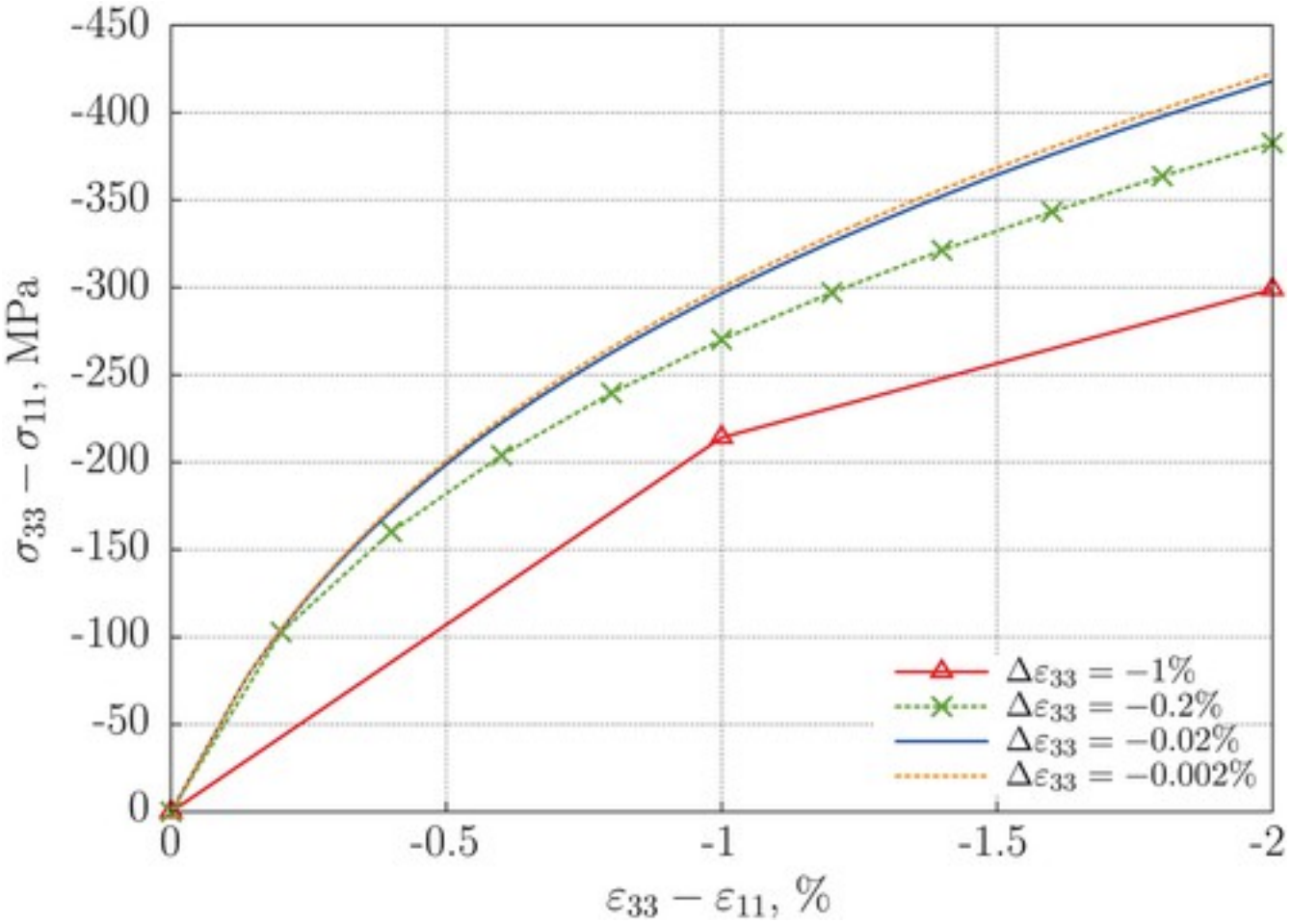

Figure 3
Open in figure viewerPowerPoint

Uniaxial compression test results with different loading rates by the cutting plane method. [Colour figure can be viewed at wileyonlinelibrary.com]
Caption

3.2.1 Error analysis

The error has been investigated on the stress changing for the same deviatoric strain loading. The test result with large strain is compared with the convergent test. The normalized error is calculated as

$$\text{Error} = \frac{\Delta\sigma_{33}}{\sigma_{33}} \times 100\% \tag{23}$$

where σ_{33} is the convergent result, while $\Delta\sigma_{33}$ is the deviation from other results to σ_{33}. The definition of the error is explained in Figure 4(a).

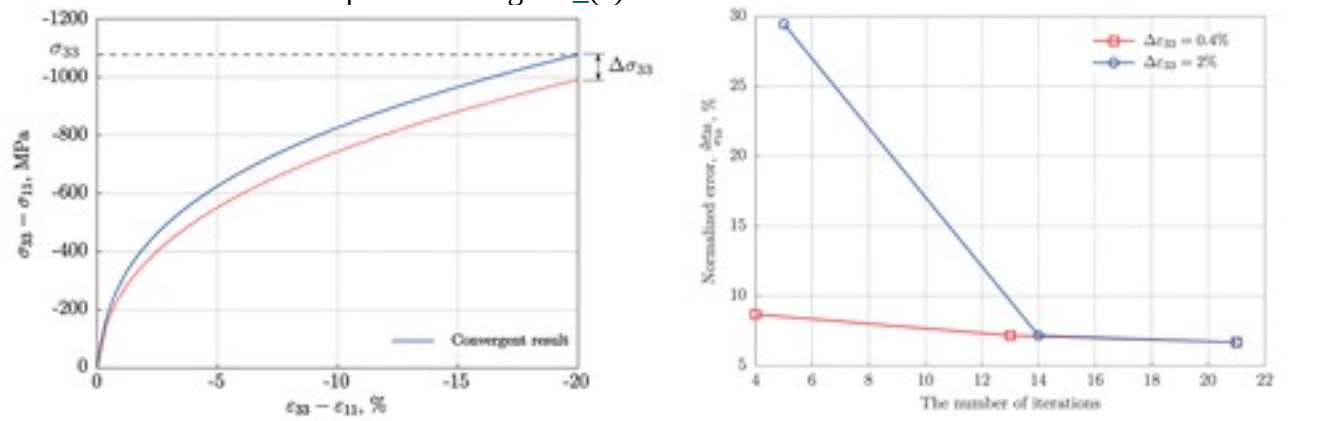

(a) The error between the simulation and the convergent result.

(b) The error changing when the iterations increase.

Figure 4
Open in figure viewerPowerPoint
The error estimation during the computation. [Colour figure can be viewed at wileyonlinelibrary.com]
Caption

In the routine, the multiplier λ determines the irreversible rate and controls the speed of the iterations. Two different strain rates ($\Delta\epsilon_{33}$=−2% and $\Delta\epsilon_{33}$=−0.4%) and three values of λ are investigated here. Based on the Figure 4(b), without the control procedure, two cases with large loading rate (−0.4% and −2%) took fewer iterations, and the errors are large (9% and 30%, respectively). By using this procedure, the error can be decreased to 7%. Therefore, changing the loading rate affects the estimation of the stress–strain relationship, and increasing the number of the iterations by changing the multiplier does decrease the error.

Therefore, in the program, a control procedure is utilized. When the deformation is larger than a certain magnitude (we use $|\Delta\epsilon|$=0.1%), the multiplier λ is decreased to increase the number of

iterations for better accuracy. If a very precise result is required, the best way is to decrease the loading rate, but it will spend much longer time on the computation.

4 Finite Element Method Simulations

The material model with CPA is implemented in a FEM code, DYNAFLOW 33. A triaxial compression is launched to check the compatibility of the new method in FEM framework. In this test, we use shale as the testing material. The calibration of parameters was performed iteratively based on the triaxial compression tests provided by ConocoPhillips 34. The calibration algorithm is an optimization method similar to the one used in 35, but we utilized a different fitness function. The optimal values of parameters were solved by minimizing the squared residuals of the distance, r_i, between experimental data, y_i, and numerical predictions, $f(\mathbf{x},\mathbf{B})$:

$$S = \sum_{i=1}^{n} r_i^2, \qquad r_i = y_i - f(\mathbf{x}, \mathbf{B}) \tag{24}$$

where **x** stands for the vector of known input variables (loading conditions and boundaries) and **B** is the vector of material parameters for calibration. The method was initialized with the mean, minimum, and maximum values of the model parameters for a triaxial compression using the DSID model. The gradient method was employed to search for the optimal parameters. The algorithm started with the initialized vector $\mathbf{B}_0$ and iteratively finds the sequence $\mathbf{B}_1$, $\mathbf{B}_2$, …$\mathbf{B}_{n+1}$ by solving

$$\mathbf{B}_{n+1} = \mathbf{B}_n - \gamma_n \nabla f(\mathbf{B}_n) \tag{25}$$

in which the value of the step size γ_n is allowed to change at each iteration. We used a series of compression tests, in which the same shale samples are under different confining stresses, as our experiment data. By using this strategy, a set of average optimal parameters is obtained, and it can represent all these samples' behavior. The material parameters are summarized in Table 3.

Table 3. Parameters in DSID model for FEM tests 32.

Elastic parameters			Free energy					Damage function		
E_0	v_0		a_1	a_2	a_3	a_4		C_0	C_1	α (-)
MPa	-		MPa^{-1}	MPa^{-1}	MPa^{-1}	MPa^{-1}		MPa	MPa	-
4.6E4	0.186		7.35E-7	1.21E-4	−3.15 E-5	2.39E-6		0.01	1.18	0.399

- DSID, deviatoric stress-induced damage; FEM, finite element method.

4.1 Axisymmetric test

A plug test is computed with FEM simulation. The size of the sample is 25.4mm ×50.8 mm cylinder suggested by the American Society for Testing and Materials (ASTM). For the efficiency of the computation, we simplify it to an axisymmetric problem (Figure 5), and we chose a quarter of the longitudinal section as the simulation domain. The radial deformations of the top surface are restricted. The left side and bottom of the domain are constrained with symmetric boundaries. A biased mesh generation is utilized so that the right top corner is refined with smaller elements. The initial confinement stress is σ_0=−27.6 MPa (4000 psi). An additional vertical stress $\Delta\sigma_2$=−160 MPa is applied.

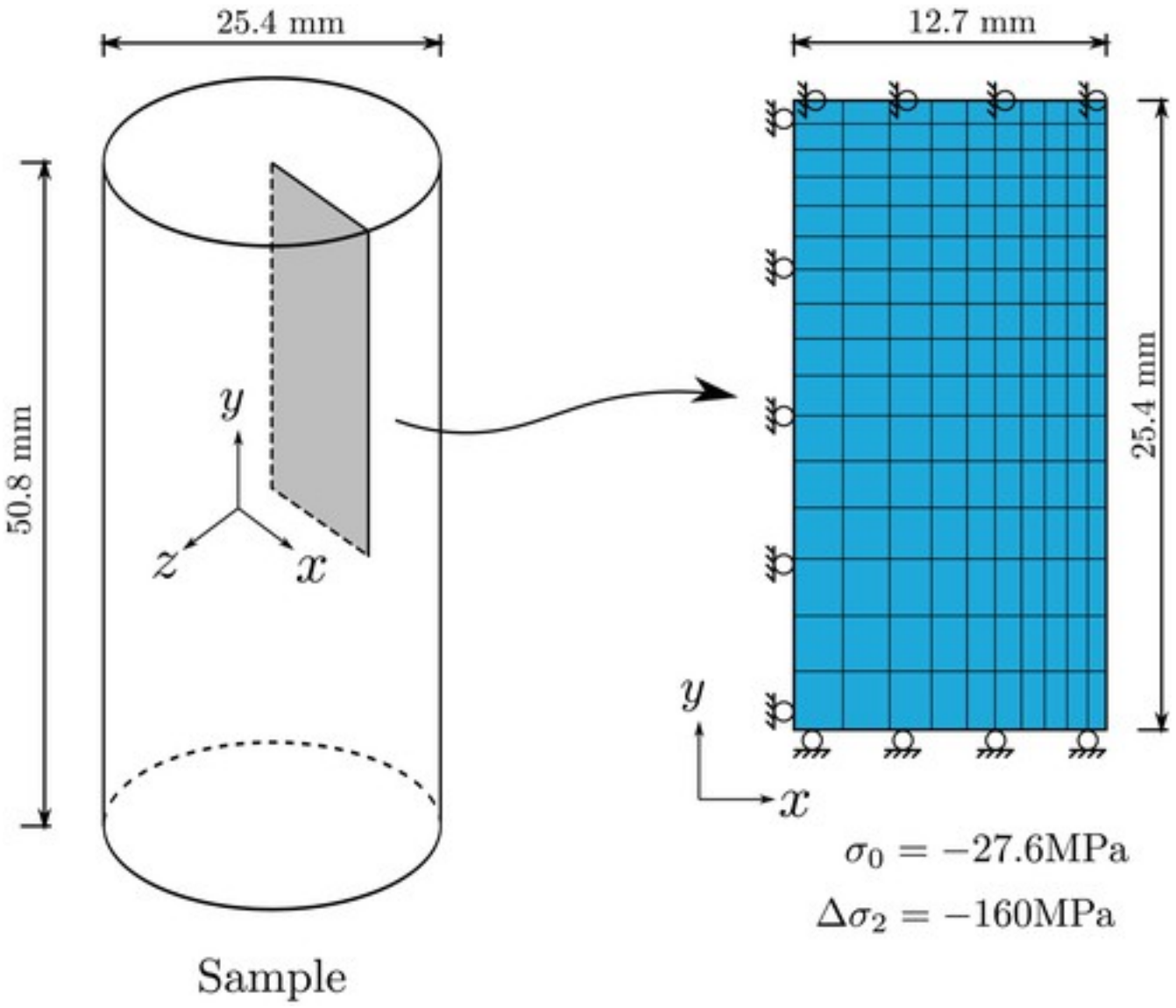

Figure 5

Open in figure viewerPowerPoint

The sketch of 2D domain for the simulation. [Colour figure can be viewed at wileyonlinelibrary.com]

Caption

The results are given by Figure 6 showing the distribution of vertical stress and horizontal damage, respectively. The fact that vertical stress is larger than horizontal stress drives cracks open vertically, which corresponds to horizontal damage. The maximum compression locates around the vertical symmetric axis, while the minimum compression is concentrated near the top right corner. Because of the constraints of the horizontal displacement on the top surface, the damage zone propagates along the 45° line from the right top corner where the maximum horizontal damage (corresponding to vertical crack) locates. Based on the results, the model with new method can be computed under FEM framework. The simulation results can capture damage

propagation in the material (Figure 6(b)). The mechanical computation with new method does not result in infinite iterations and always remains stable. However, some integration points may have large residual force.

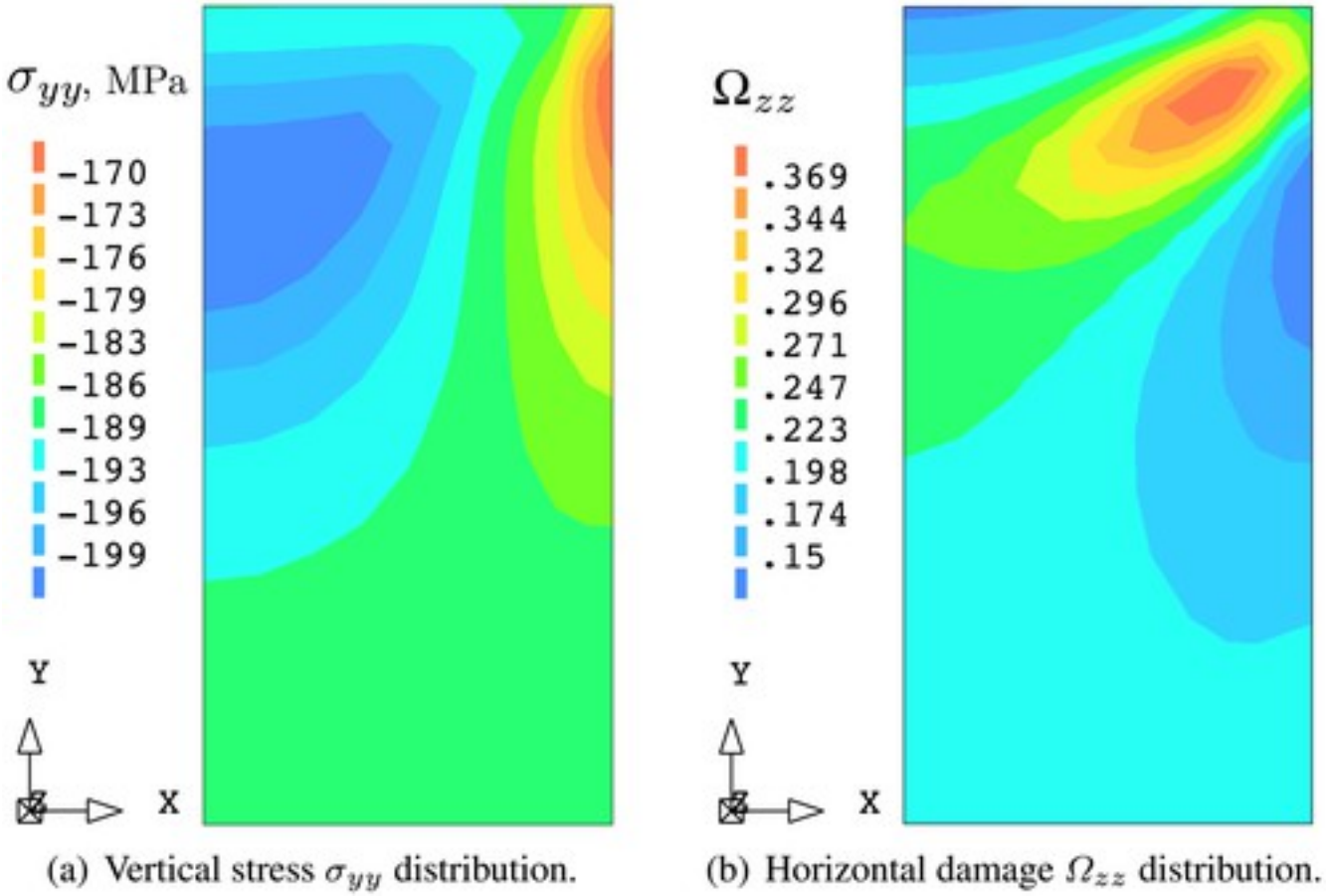

(a) Vertical stress σ_{yy} distribution. (b) Horizontal damage Ω_{zz} distribution.

Figure 6

Open in figure viewerPowerPoint

Simulation results of a plug test. [Colour figure can be viewed at wileyonlinelibrary.com]

Caption

5 Fluid Diffusion in Shale

5.1 Poromechanics

Shale is one type of sedimentary rocks in the organic matter. In general, it is saturated with the fluid underground. After shales are drilled out, this easily weathered rock must be kept in moisture environment. Therefore, samples of shales usually contain fluids inside, and the effects of fluid pressure must be considered in experiments and simulations. Based on the theory of poromechanics 27, for an isothermal saturated porous solid , stresses and pressures are governed by

1. Equilibrium equations:

$$\nabla \cdot \boldsymbol{\sigma} + \rho \boldsymbol{g} = \mathbf{0} \quad \boldsymbol{\sigma} = \boldsymbol{\sigma}' - b\, p_f \boldsymbol{\delta} \tag{26}$$

2. Mass balance equation:

$$\frac{\mathrm{d}}{\mathrm{d}t}(\rho_f \phi) + \nabla \cdot (\rho_f \boldsymbol{q}_f) = 0 \tag{27}$$

where the Darcy flux is

$$\boldsymbol{q}_f = -\frac{k}{\mu_f}\left(\nabla p_f - \rho_f \boldsymbol{g}\right) \tag{28}$$

3. Porosity equation:

$$\frac{\mathrm{d}\phi}{\mathrm{d}t} = b\nabla \cdot \boldsymbol{v}^S + \frac{1}{N}\frac{\mathrm{d}p_f}{\mathrm{d}t} \qquad \frac{1}{N} = \frac{b-\phi_0}{K_S} \tag{29}$$

For a slightly compressible fluid, the balance equation and the porosity equation can be combined to yield the following pressure equation 36:

$$\frac{1}{M}\frac{\mathrm{d}p_f}{\mathrm{d}t} + \nabla \cdot \boldsymbol{q}_f + b\nabla \cdot \boldsymbol{v}^S = 0 \qquad \frac{1}{M} = \frac{1}{N} + \frac{\phi}{K_f} \tag{30}$$

where $\boldsymbol{\sigma}$ is the total Cauchy stress, $\boldsymbol{\sigma}'$ is the effective stress, $b = 1 - \frac{K^S}{K_S}$ is the Biot coefficient 37, $\rho = \rho_s(1-\phi) + \rho_f\phi$ is the total mass density, ρ_s is the solid mass density, ρ_f is the fluid mass density, ϕ is the porosity, ϕ_0 is the initial porosity, $\boldsymbol{g}$ is the body force, k is the permeability, μ_f is the fluid viscosity, $\boldsymbol{q}_f$ is the Darcy flux, K_s is the solid bulk modulus, and K_f is the fluid bulk modulus. The diffusion time is controlled by the following diffusion coefficient 27, 38

$$c_f = \frac{k}{\mu_f} M \frac{\lambda^S + 2\mu^S}{\lambda^S + 2\mu^S + b^2 M} \tag{31}$$

where λ^s and μ^s are the lame constants of solid skeleton. In our case, c_f=9.154 × 10^{-9} m^2/s. The time can be computed as

$$t = \frac{T H^2}{c_f} \tag{32}$$

in which T is the time factor and H is the length of the drainage path. Based on different time factors, we will have different loading rates for drainage. Short time corresponds to a fast loading (‘undrained’ test), while longer time refers to a slow loading (‘drained’ test) 39. Although the external loadings in both tests are the same, because of the effective stress and pore pressure, the responses of samples are distinct. To account for the drainage of the fluid in shales under loading, the top and cylindrical surfaces are constrained with zero fluid pressure (Figure 7). The elements on the drainage boundaries are refined for better accuracy. In these simulations, we use 3D geometries for solving 3D problems.

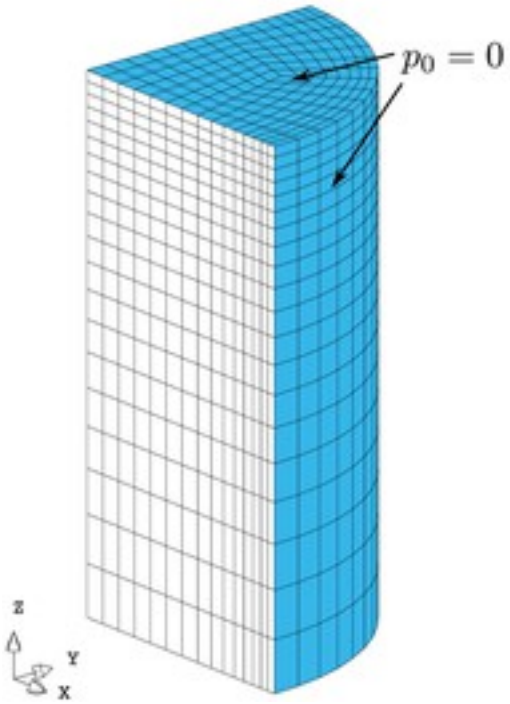

permeability	$k = 1.71 \times 10^{-21}$ m^2
viscosity	$\mu_f = 10^{-9}$MPa· s
fluid bulk modulus	$K_f = 2.17$ GPa
porosity	$\phi = 0.3$
drainage path	$H = 0.0127$ m
diffusion coefficient	$c_f = 9.154 \times 10^{-9}$ m^2/s

Figure 7

Open in figure viewerPowerPoint

3D mesh used for simulations with fluid diffusion. [Colour figure can be viewed at wileyonlinelibrary.com]

Caption

5.1.1 Slow loading test

The time increment related to the slow loading (‘drained case’) is

$$\mathrm{d}t = \frac{10^2 H^2}{c_f} = 1.76 \times 10^6 \text{ s} \approx 20 \text{ day} \tag{33}$$

The deviatoric loading is −100 MPa in this simulation. Results are displayed in Figure 8. From Figure 8(c), the fluid pressure is negligible compared with the magnitude of the stress σ_{zz}, so the effective stress $\sigma zz'$ is almost equal to the total stress σ_{zz}. The result of the effective stress is close to the result of the dry test in Section 4.1 when it reaches −100 MPa deviatoric loading.

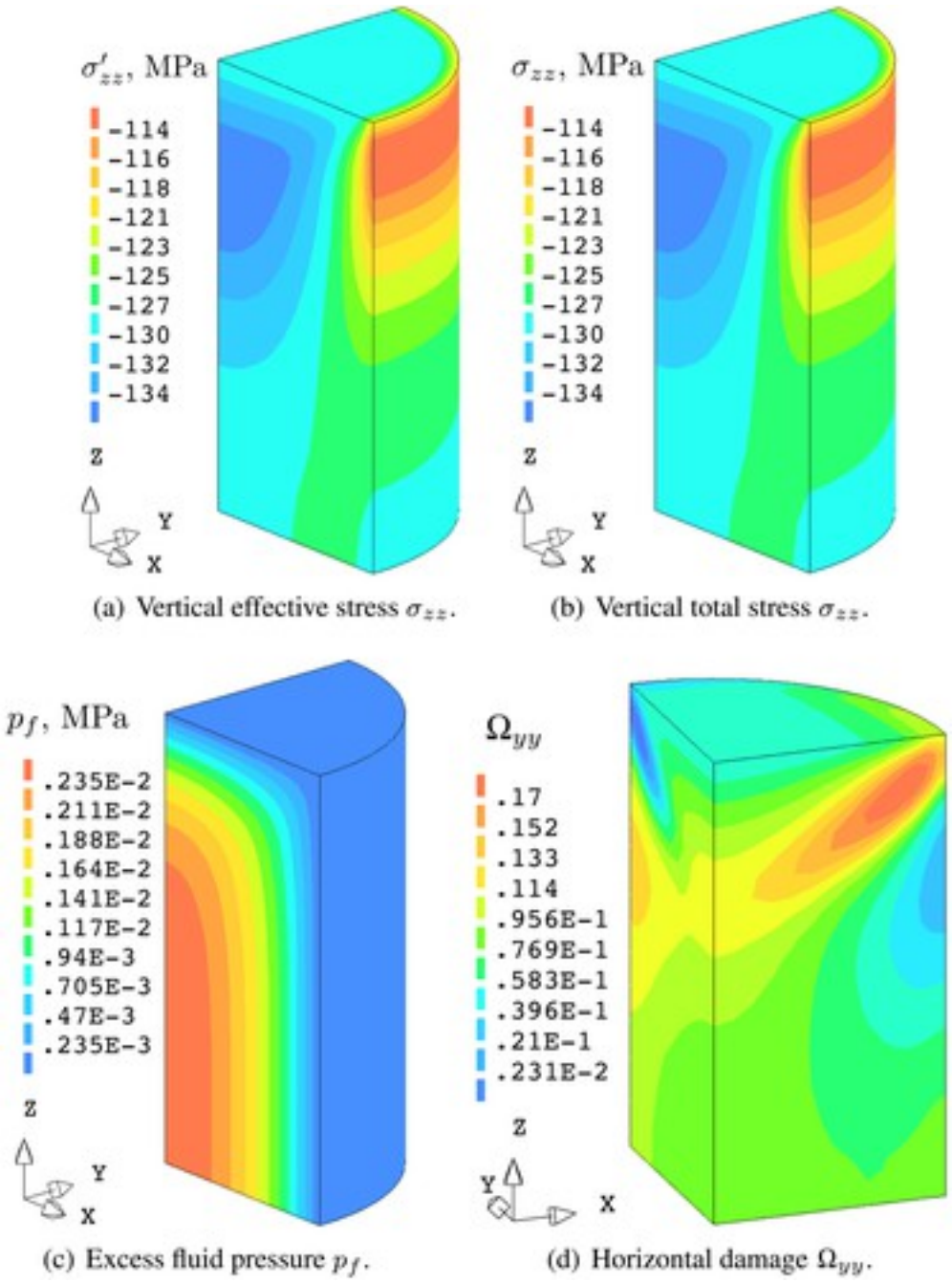

(a) Vertical effective stress σ_{zz}. (b) Vertical total stress σ_{zz}.

(c) Excess fluid pressure p_f. (d) Horizontal damage Ω_{yy}.

Figure 8

Open in figure viewerPowerPoint

Simulation results of the slow loading (‘drained’) test. [Colour figure can be viewed at wileyonlinelibrary.com]

Caption

5.1.2 Fast loading test

Normally, the laboratory test is taken for 1 or 2h, which means that the experiment is fast loading test (‘undrained’ test). This simulation can be launched with smaller time period. The time increment related to the fast loading is

$$\mathrm{d}t = \frac{10^{-2} H^2}{c_f} = 176\,\mathrm{s} \approx 3\,\mathrm{min}. \tag{34}$$

The deviatoric loading is −100 MPa in this test as well. The excess fluid pressure increases to 9MPa inside the sample (Figure 9(c)), which redistributes the stresses response of the sample and decreases the effective stresses. Because of the drainage boundary, the gradient of the excess pore pressure is high near the drainage surfaces. Compared with the ‘drained case’, the total compressive stresses increase while the effective compressive stress decreases because of the effect of fluid pressure (Figure 9(b,a)).

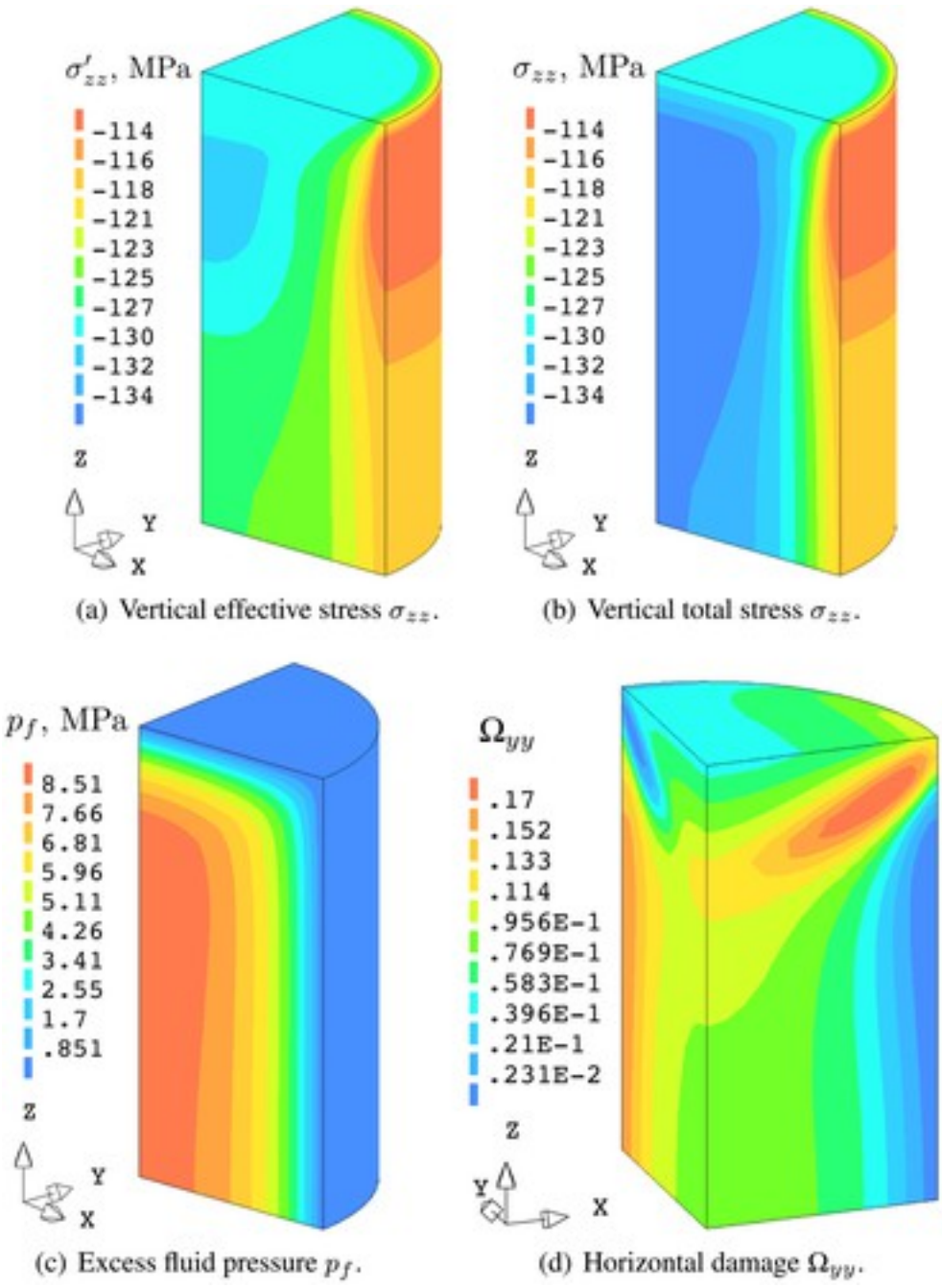

(a) Vertical effective stress σ_{zz}. (b) Vertical total stress σ_{zz}.

(c) Excess fluid pressure p_f. (d) Horizontal damage Ω_{yy}.

Figure 9

Open in figure viewerPowerPoint

Simulation results of the fast loading (‘undrained’) test. [Colour figure can be viewed at wileyonlinelibrary.com]

Caption

5.1.3 Fully undrained test

One extreme case of the fast loadings is the fully undrained test, in which there is no drainage on the boundaries. The simulation results of the fully undrained test are plotted in Figure 10.

Because of the displacement constraints of the top surface, the high fluid pressure is induced around the top arc edge, and it spreads along 45° into the center of the sample (Figure 10(c)). However, inside the sample, the fluid pressure is compressive. This highly inhomogeneous fluid pressure may make the computation crash earlier than the slow and fast loading tests at higher external loadings.

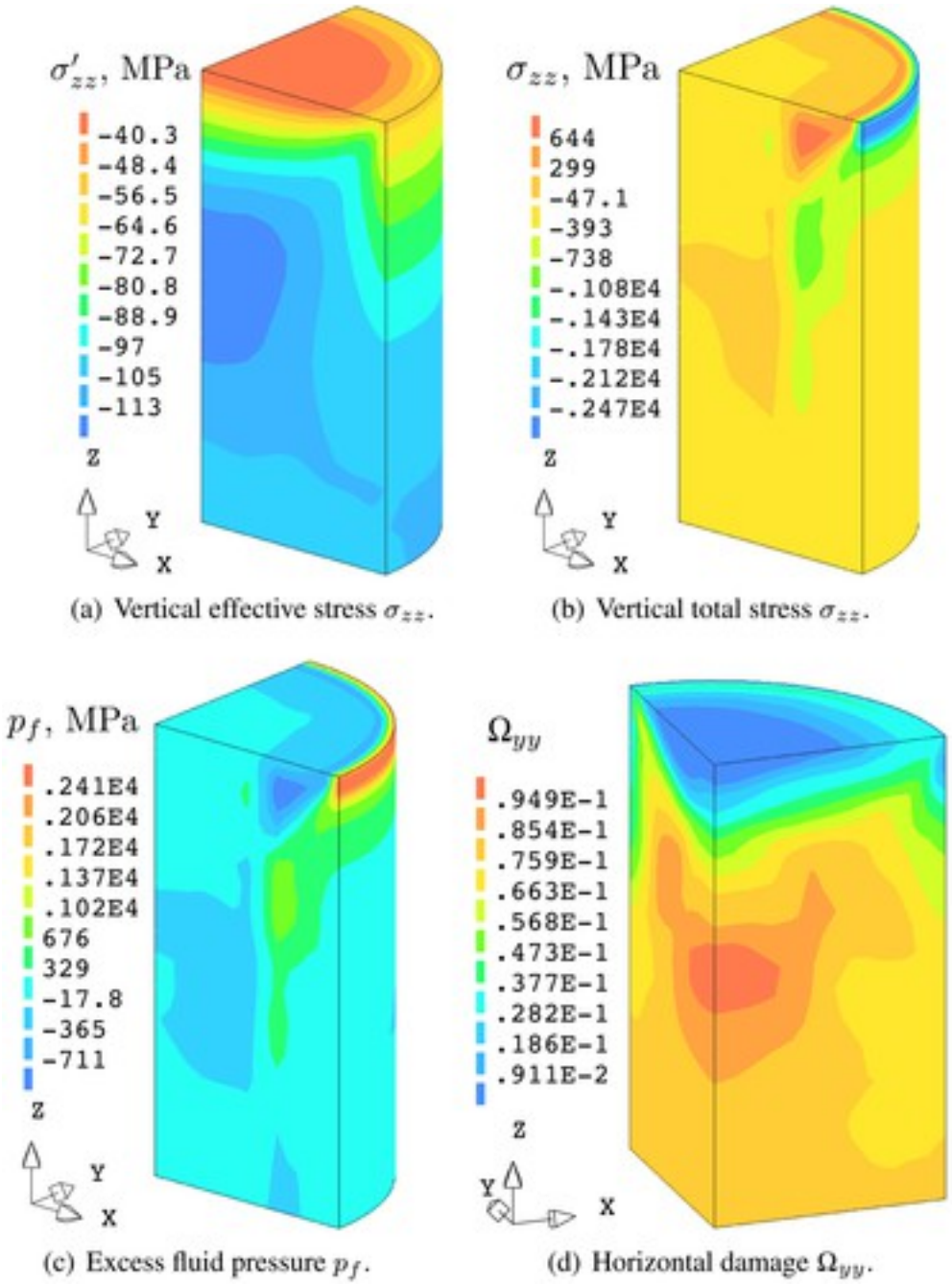

(a) Vertical effective stress σ_{zz}. (b) Vertical total stress σ_{zz}.

(c) Excess fluid pressure p_f. (d) Horizontal damage Ω_{yy}.

Figure 10

Open in figure viewerPowerPoint

Simulation results of the fully undrained test. [Colour figure can be viewed at wileyonlinelibrary.com]
Caption

5.1.4 Discussion and error estimation

The external loadings versus vertical strains of samples are plotted in Figure 11 for the slow and fast loading cases as well as the fully undrained case and the simulated result with calibrated material parameters. During the laboratory experiment setup, the sample is sitting for a while with initial confinements, so the excess pore pressure is assumed to be dissipated after this sitting time. The simulation results indicate that the initial response of samples is close to the slow loading (which is especially clear when cumulative strain from −0.1% to −0.2%). At the deviatoric loading step, the rate of loading is fast ($\Delta\epsilon_{33}$=0.001%/s), so the fluid does not drain out instantly. When the loading increases, excess fluid pressures are induced in the sample. Therefore, at this stage, the sample behavior is close to the response of fast loading case. The fully undrained case predicts higher strength than the other cases, and the response is also distinct compared with the others.

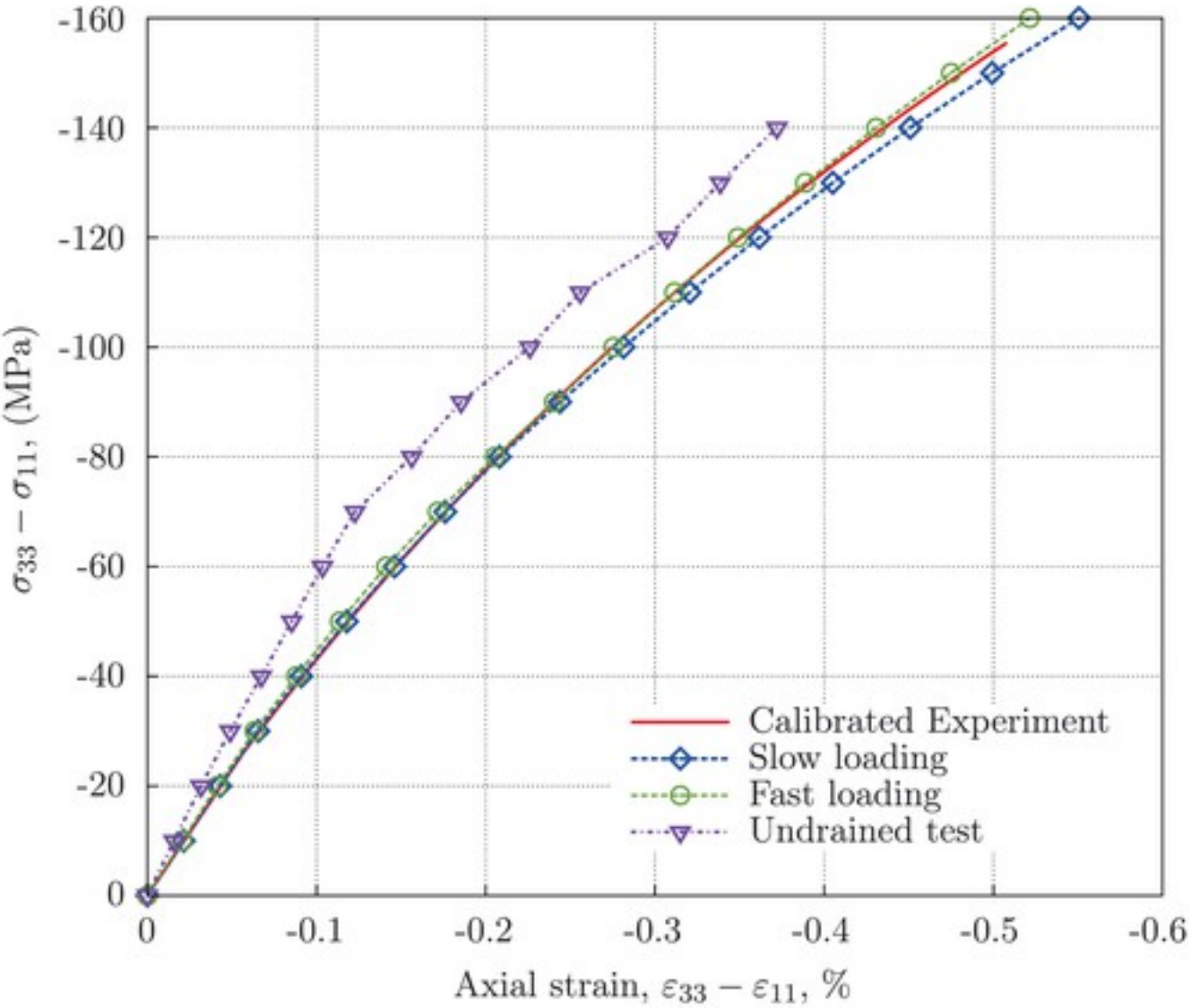

Figure 11

Open in figure viewerPowerPoint

The stress–strain curves of the calibrated experiment, fast loading, slow loading tests, and undrained test. [Colour figure can be viewed at wileyonlinelibrary.com]

Caption

Damage is associated with the effective stress sustained by rock matrix. In Figure 8(c) for the slow loading case, the vertical effective stresses is close to the total one, so the magnitude of horizontal damage Ω_{yy} is as high as the dry case. However, the vertical effective stress obtained in Figure 9(c) for the fast loading test is less than slow loading test, which redistributes the horizontal damage on the vertical drainage boundary. Finally, in Figure 10(c) for the fully undrained test, since the extremely high excess pore pressure is induced, the vertical effective stress reduces to a low level, and the magnitude of horizontal damage is one order smaller than the others.

The fast loading and slow loading are compared with the fully undrained case by the equation

$$\text{Error} = \frac{\sigma_{f/s} - \sigma_{ud}}{\sigma_{ud}} \times 100\% \quad (35)$$

where $\sigma_{f/s}$ is the stress given by the fast loading or the slow loading test and σ_{ud} is the stress obtained by the fully undrained test. As obtained in Figure 12, the errors for both fast and slow loadings decrease from 25% to 10%. Compared the fast loading with the slow loading from Figure 12, the error at the starting point is large, then it reduces at the middle of the test. The initial error is because of the disturbing of the loading imposed by experiment instruments, which is not easy to remove from the calibration for laboratory tests. This error decreases when the loading increases. After the middle point, because of the aggregation of the excess pore pressure, the sample behaviors like under 'undrained' condition (fast loading case). Consequently, the difference between the slow loading and fast loading increases.

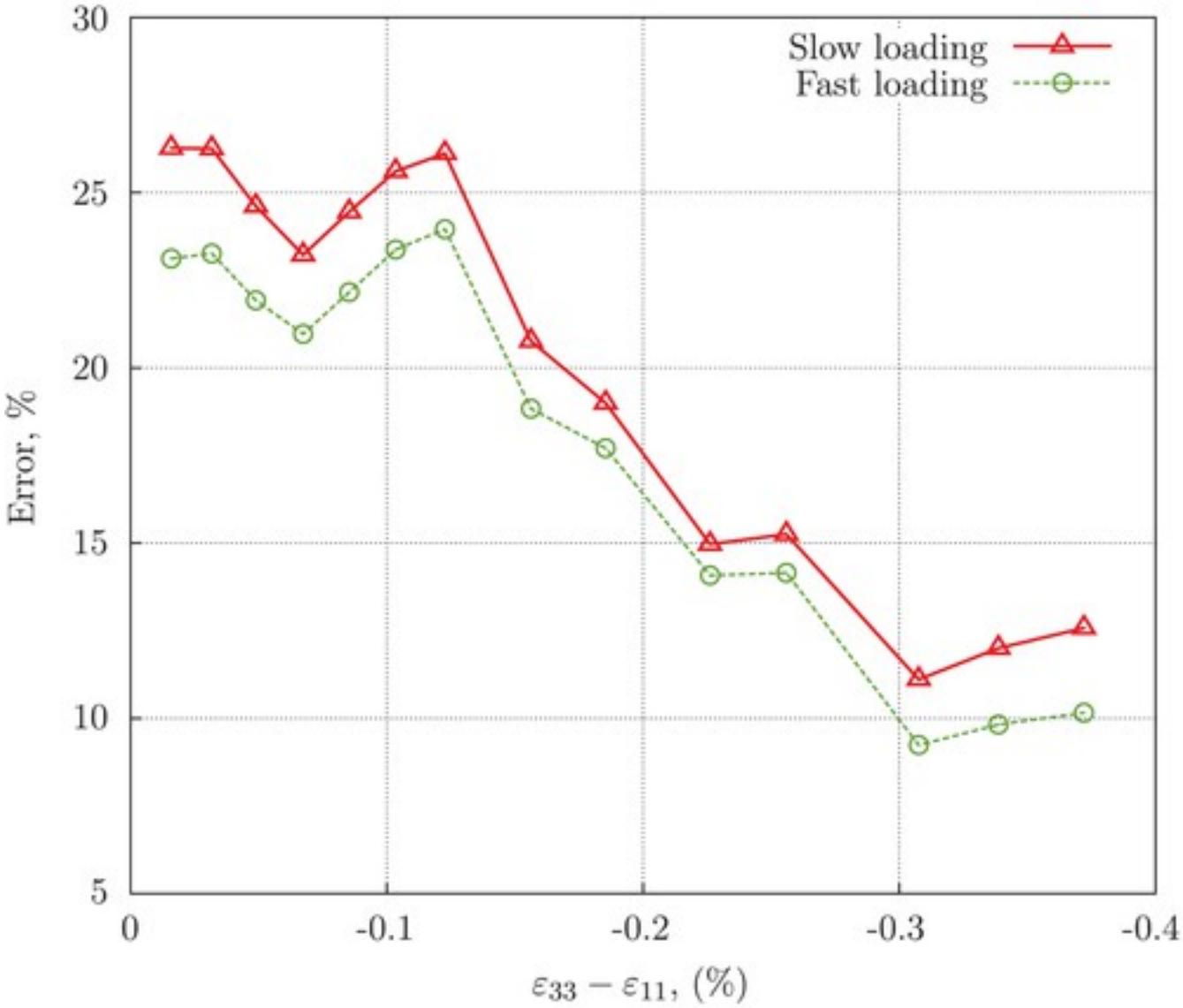

Figure 12

Open in figure viewerPowerPoint
The errors with respect to the undrained case for slow and fast loadings. [Colour figure can be viewed at wileyonlinelibrary.com]
Caption

6 Conclusion

A proposed procedure has been implemented with cutting plane algorithms to solve the nonlinear equations for the continuum damage model. The accuracy of the new method has been investigated, and the results indicate that the new version improves the stability of the computation of the constitutive model. The new procedure is proved to be capable to incorporate with FEM codes to solve geomaterial problems. A 2D axisymmetric representation of a plug test for shale is simulated with the damage model. Because of the constraints of the top horizontal displacements, the concentration of the vertical stress is found near the top edge of the sample, where the horizontal damage is generated as well. The high damage propagation zone is inclined at 45°.

Because shale is usually saturated with fluids underground, the sample of shale is moisturized. The fluid diffusion in shale experiments has been investigated in 3D meshes with various loading rates and drainage boundaries, such as the slow loading, fast loading, and fully undrained tests. The results illustrate at the beginning that the response of the experiments is close to the slow loading, then it changed to the behavior under the fast loading condition. Because of the high excess pore pressure, the vertical effective stresses are reduced so that the horizontal damage also decreases.

Further studies will be dedicated to the coupled effects of hydraulic, mechanical, and damage effects on rock properties such as permeability and bulk modulus. This research work is expected to bring new insights in hydromechanical damage modeling in rocks, for possible applications on geomechanic problems.

Acknowledgement